Ke-Jung Huang
Department of Mechanical Engineering,
National Taiwan University,
Taipei 106, Taiwan
e-mail: b95502111@ntu.edu.tw

Shen-Chiang Chen
Department of Mechanical Engineering,
National Taiwan University,
Taipei 106, Taiwan
e-mail: b94501023@ntu.edu.tw

Haldun Komsuoglu
Robolit LLC,
1829 Pine Street, Suite 404,
Philadelphia, PA 19103
e-mail: haldun.komsuoglu@gmail.com

Gabriel Lopes
Delft Center for Systems and Control,
Delft University of Technology,
Delft 2628, The Netherlands
e-mail: G.A.DelgadoLopes@tudelft.nl

Jonathan Clark
Department of Mechanical Engineering,
Florida State University,
Tallahassee, FL 32310
e-mail: jeclark@fsu.edu

Pei-Chun Lin[1]
Mem. ASME
Department of Mechanical Engineering,
National Taiwan University,
Taipei 106, Taiwan
e-mail: peichunlin@ntu.edu.tw

Design and Performance Evaluation of a Bio-Inspired and Single-Motor-Driven Hexapod Robot With Dynamical Gaits

Over its lifetime, the hexapedal robot RHex has shown impressive performance. Combining preflexes with a range of control schemes, various behaviors such as leaping, running, bounding, as well as running on rough terrain have been exhibited. In order to better determine the extent to which the passive and mechanical aspects of the design contribute to performance, a new version of the hexapedal spring-loaded inverted pendulum (SLIP)-based runner with a novel minimal control scheme is developed and tested. A unique drive mechanism is utilized to allow for operation (including steering) of the robot with only two motors. The simplified robot operates robustly and it exhibits walking, SLIP-like running, or high-speed motion profiles depending only on the actuation frequency. In order to better capture the critical nonlinear properties of the robot's legs, a more detailed dynamic model termed R2-SLIP is presented. The performance of the robot is compared to the basic SLIP, the R-SLIP, and this new R2-SLIP model. Furthermore, these results suggest that, in the future, the R2-SLIP model can be used to tune/improve the design of the leg compliance and noncircular gears to optimize performance.
[DOI: 10.1115/1.4029975]

1 Introduction

Most ground animals have evolved with agile and robust legs, allowing them to elegantly and rapidly negotiate uneven terrain. How animals coordinate their many body joints, however, remains a mystery. Because it has proven difficult to mimic their amazing locomotion capabilities, research on legged robotics has taken two basic approaches: One is to build robots with few active degrees of freedom (DOFs) and use them to generate animal-like dynamic locomotion; the other is to build robots with a large number of DOFs and to explore rough terrain negotiability with quasi-static locomotion. Perhaps in the near future these two approaches can be merged, and robots will perform rapid locomotion on natural terrain just as animals do.

The study of dynamic locomotion of robots was initiated by the development of monopods in the 1980s [1]. Around the beginning of the third millennium various dynamical multilegged robots were developed, examples include the quadruped Scout series [2,3], quadruped Tekken series [4,5], hexapod Sprawl series [6–8], hexapod RHex [9–13], EduBot [14,15], and VelociRoACH [16]. In order to generate dynamic locomotion, these robots have one common yet important characteristic—compliant components which allow kinetic energy to be stored and released from the potential strain energy of the component. These springs help compensate for the insufficient power density of commercial joint actuators (i.e., electric motors) and enable the robot to match the center of mass locomotion characteristics of animals. Researchers have found that, even though their morphologies vary significantly, animals' dynamic running locomotion in the sagittal plane can be approximated by a simple mathematical model: the "SLIP" model [17–20]. Here, the animal's body is treated as a point mass and its legs are approximated by a massless linear spring. As a running "template," the SLIP model provides a prescriptive control guidance to the original complex biological or robotic systems which represent empirical "anchors" by specifying the actuation, joints, and rigid structures [21]. Thus, in the past few decades, the success in developing dynamic behavior for legged robots has commonly been judged by the similarity of the robot's motion characteristics to that of the SLIP model. For example, though the hexapod RHex has only one active rotational DOF per leg, it can generate SLIP-like jogging behavior through carefully matching the actuation at the hip joints and the passive compliant legs [22,23]. In addition, RHex also has good ability to negotiate rough terrain because of its full-rotation leg reposition strategy. Similarly, the hexapod iSprawl has carefully tuned leg compliances, and it can be driven by a single motor and generate SLIP-like locomotion, though without the same ability to clear obstacles [7].

Here, following our initial presentation at Ref. [24], we report on the complete development of a simple hexapod robot which is driven by only one motor but which can perform dynamic running locomotion as well as negotiate rough terrain. The conceptual design of the robot lies in the intersection of two robots: the

[1]Corresponding author.
Manuscript received July 17, 2014; final manuscript received March 3, 2015; published online April 14, 2015. Assoc. Editor: Jaydev P. Desai.

simple morphology of RHex with bio-inspired tripod gaits [9]; as well as the single-motor transmission strategy of iSprawl [7]. The key to this intersected design lies in the use of a noncircular gear pair in the transmission system, which allows the input and output gears to have varied speed profiles to create an adequate tripod running gait using a single-motor input. Besides the driving motor, the robot also has a small servo motor for turning. Thus, the robot only has two active DOFs for locomotion, and the control policy of one turning and one driving DOF on the robot is identical to most wheeled vehicles. The use of properly tuned compliant legs, however, allows the mechanism to achieve complex behaviors with low DOFs. In our scenario, we show that a specialized 2DOF robot that resembles a nonholonomic system is capable of traversing both flat ground (3DOFs) and rough terrain (typically described in 3D space, 6DOFs).

It has been shown time and again that in biological systems there is a tight coupling between the neural (active) and musculoskeletal (passive) parts of the body [25,26]. In contrast, a typical robot design considers the active and passive aspects of the system separately. First, the electromechanical structure is constructed. Then a control algorithm is established to force the passive construct to perform in the desired manner. This approach often gives rise to systems that are rigid, slow, and inefficient. Inspired by observations in biology, RHex, with its half-circle compliant legs and task-level open-loop control algorithm, was the first mobility platform where the passive and active aspects of the system are considered in tandem for the common goal of producing efficient and stable locomotion. The "behavioral control" in RHex is not confined to the software but is also "embedded" into the components of the passive body. This holistic approach in behavioral controller design, which was later successfully demonstrated in systems such as Sprawl [8] and RiSE [27], is a powerful idea that we would like to better understand and establish guidelines for. The single-motor hexapod presented in this paper is another step in this direction. Here, the authors experimentally investigate how the generation of excitation in a dynamic locomotion system can be further embedded into the passive mechanism. With its reduced number of motors and circuitry, the resulting platform demonstrates a low-cost version of a RHex-class system which may find applications in fields spanning entertainment to education. More importantly, it allows us to study the pros and cons of heavier use of passive components in behavioral control.

The design of the robot starts with understanding the dynamic motion of the SLIP model and then expands the morphology of the monopod to the hexapod structure, which can be operated in intrinsically robust "tripod posture" (i.e., having three legs stand on the ground) at any moment by means of the worm and worm gear pairs and noncircular gear pairs utilized in the transmission system. The former allows the robot to stand without powering the motor because of its nonbackdrivable characteristics. The latter provides the feasibility of setting desired periodic leg speed profiles and phase offsets, so the proper alternating tripod gait for dynamic locomotion can be generated.

This intentional mechanical locking of the drive train shifts the focus of the control of the robot onto the passive dynamics of the compliant structure. Body compliance can be achieved by either direct use of a passive spring, by simulating the multi-DOF system to act like a spring [28], by mixing the two [29], or by using a stiffness-tunable passive springy leg [30]. While many compliant leg designs have been reported, evidence suggests that a nonlinear stiffness [31] and a rolling contact helps locomotion [32]. Since a leg with a circular shape has these attributes, is easy to fabricate, and has a history of use on other robots, it was adopted in the final robot design.

The locomotion behavior of this robot was then compared to three reduced-order models: SLIP, the R-SLIP model, and the new R2-SLIP model. The first is the original design basis of the robots, and the latter two capture characteristics of the circular leg including rolling behavior and change of leg stiffness during locomotion. The R-SLIP model was previously developed in our lab and was based on the morphology of the half-circular leg [33]. The R2-SLIP is a revised version of the R-SLIP model with an additional passive spring; the details of which are described in the Appendix. Note that though the SLIP model can be set to have changeable stiffness, it cannot create rolling behavior (forwarding ground contact point) within its morphology. Although several new reduced-order models have recently been developed as well (such as CT-SLIP [34], SLIP-R [35], C-Pod [36], M-SLIP [37] ASLIP [28], and SLIP-T [38]), they are either at a more abstract level or fit to some specific form of leg. As a result, the R-SLIP and R2-SLIP models are adopted for performance comparison since they originated from the circular leg used on the robot, and have a similar simple structure as the SLIP. Thus, the use of this simplified, mechanical robot allows for a focused evaluation of the role of passive dynamics (specifically leg design) in creating fast, stable, SLIP-like dynamical running.

The remainder of the paper is organized as follows: Sec. 2 describes the robot design process. Sections 3 and 4 report the design of the noncircular gear pair and leg, respectively. Section 5 briefly describes the R-SLIP and R2-SLIP models and their parameter mapping to the robot. Section 6 reports the results of experimental evaluation, and Sec. 7 concludes the work.

2 Robot Design Process

As mentioned in the introduction, the SLIP model depicted in Fig. 1(*a*) is widely used as the sagittal-plane running template of biological systems. The model has three system parameters: length of the spring (l); stiffness of the spring (k); and mass (m). The SLIP model exhibits a set of stable periodic trajectories that include stance and flight phases.

The dynamics of the SLIP model in stance phase can be represented as

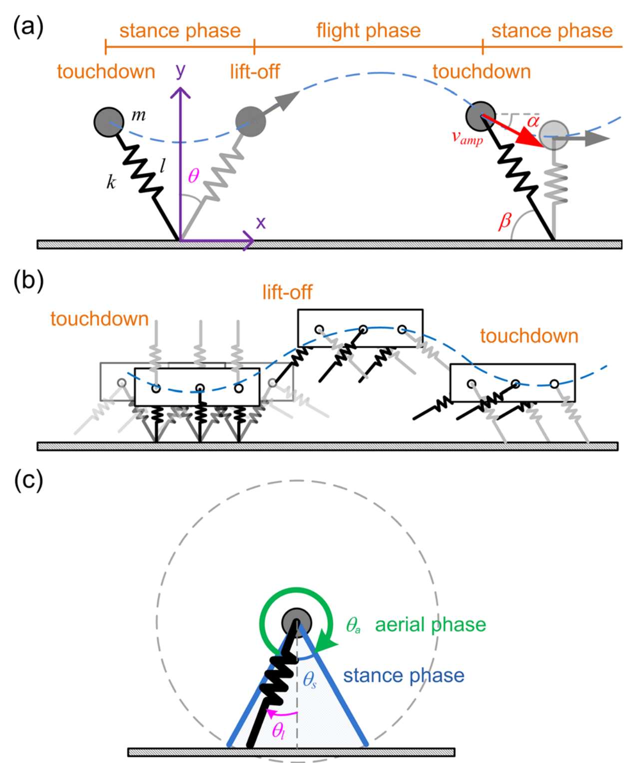

Fig. 1 The model and the robot. (*a*) The SLIP model with its intrinsic parameters, ICs, and motion profile. (*b*) The robot performs dynamic motion similar to the SLIP model, which includes a stance phase and a flight phase. (*c*) The leg motion profile, which includes a stance phase and an aerial phase.

$$
\ddot{\theta} = \frac{1}{l}(g\sin(\theta) - 2\dot{l}\dot{\theta})
$$

$$
\ddot{l} = l\dot{\theta}^2 - \frac{k}{m}(l - l_0) - g\cos(\theta) \tag{1}
$$

where l_0 and g are the natural length of the spring and gravitational constant. Together with the initial conditions (ICs) given at the moment of touchdown, the model's quantitative motion versus time can be solved numerically. The ICs are represented in states associated with the mass and leg motion, including landing angle (β), touchdown speed (v_{amp}), and touchdown angle (α) included by the touchdown velocity and horizontal line as shown in Fig. 1(*a*). When the ICs are appropriately chosen, the model keeps moving forward while the spring compresses and releases, and at a certain moment the model takes off and starts its flight phase [20]. The dynamics of the SLIP model in flight phase are ballistic and are affected by gravity alone. After the ballistic flight, the SLIP model with the same landing angle touches down on the ground again and starts its next stance phase. The motion of the model is alternated by these two phases as shown in Fig. 1(*a*).

Equation (1) reveals that spring dynamics are affected by three factors: (i) centrifugal force; (ii) elasticity of the leg; and (iii) gravity. If the variation of angle and its derivative, θ and $\dot{\theta}$, are both small, the factors (i) and (iii) only affect the equivalent point of the leg, and the period of the leg is only determined by factor (ii). In this case, the equation of motion of the model can be simplified as

$$
\ddot{l} = -\frac{k}{m}(l - l_0) - g \tag{2}
$$

and its solution can be derived as

$$
l(t) = c_1 \sin\left(\sqrt{\frac{k}{m}}t + \delta_p\right) + c_0 \tag{3}
$$

where δ_p, c_0, and c_1 are constants. The model moves vertically, so in this case it acts like a 1D hopper, a reduced-order 1DOF model of the original two-dimensional SLIP model. This 1D model will be used to roughly estimate the proper relation between leg stiffness and mass.

Although the SLIP model can adequately serve as the template of the original complex robot (i.e., anchor) [21], there remain several key discrepancies which should be taken into account during the design process. First, the SLIP model is a planar point-mass system which has only 2DOFs. In contrast, the physical robot is better modeled as a rigid-body system (i.e., with inertia) which moves in 6DOF space. Even when the robot's mapped 2DOFs are controlled to generate motion similar to the model, the other 4DOFs should be taken care of to reduce their effect on the two controlled DOFs. Second, the SLIP model is energy conservative. In contrast, the physical robot is an energy-dissipative system that requires an onboard energy source. To remedy these discrepancies, the robot should have multiple actuated legs.

Together with the passive compliant leg, the overall hexapedal morphology of the robot is similar to that of RHex [9], but it has different methods of actuation and leg coordination. The use of an alternating tripod gait and compliant legs has several advantages: (i) The mapping from three real and synchronously moving legs of one tripod to one virtual leg of the SLIP model is straightforward, where the spring constants of the former can be summed up and roughly equated to that of the latter. (ii) Geometrically, it is also reasonable to locate the virtual leg right below the COM where the middle real leg is located. (iii) During the tripod stance phase, the moments generated from the foreleg and hindleg normal to the sagittal plane can cancel out each other. Thus, if the robot touches the ground without any pitch angle, ideally it will maintain the same configuration at lift-off. This characteristic keeps the robot's COM motion in the sagittal plane and close to the reduced-order SLIP model.

The motions of the two tripods should be coordinated in a specific manner, so the robot can exhibit dynamic locomotion with flight phases. The leg motion has the following constraints: (i) The time duration of a tripod in its aerial phase, T_{a}, should be longer than its stance phase, T_{s}, so that the time duration can include the stance phase of the other tripod and the two flight phases, T_{f}, of the robot in between

$$
T_{\mathrm{a}} = T_{\mathrm{s}} + 2T_{\mathrm{f}} \tag{4}
$$

(ii) The configuration and motion of the tripod in stance phase should sweep through a certain angle range, θ_{s}. Thus, a mechanism should be designed to transform the continuously rotating motor motion to the reciprocating leg motion described above. A linkage mechanism is one obvious choice. However, this method provides limited ground clearance. To enhance the robot's ability to negotiate obstacles, the leg motion is designed to continuously rotate in the same direction as the motor input, but the phase mapping from motor to leg is altered. Thus, when the motor moves at constant speed, the leg can still move according to a specific pattern as described above. The time duration of the leg in aerial phase is roughly 1–1.5 times that in stance phase, and the rotation angle of the leg in flight phase, θ_{a}, is about 6 times greater than in stance phase, θ_{s}. As a result, the leg rotational speed in the aerial phase is at least 4–6 times higher than in the stance phase. This varying rotation speed can be achieved by the use of noncircular gears, which vary the speed ratio and move periodically. In addition, the two tripods should move alternately, and this phase difference can be achieved by offsetting the orientation of the gears. As a result, the robot can be driven by a single motor without position control effort, yet achieve the desired trajectories. An illustrative sketch of the robot's locomotion is provided in Fig. 1(*b*).

A commercial DC motor is adopted as the source of mechanical power. Because the motor's high-speed and low-torque characteristics are the opposite of the desired low-speed and high-torque leg motion, a transmission with high-speed reduction is required between the motor and the noncircular gear pairs. The nominal speed of the motor can be easily found in its datasheet, and the leg stride frequency is designed based on the behavior of a mammal with similar weight. Previous research indicates that the stride frequency in animals varies from about 1 to 6 Hz (mouse to horse), and that larger mammals have even lower stride frequencies [39]. The stride frequency of a 0.36 kg rat while jogging is about 1.5–5 Hz, and that of a 9.2 kg dog is about 2–4 Hz. The robot's weight is targeted around 3 kg, so the stride frequency is set at about 3–4 Hz. To successfully excite SLIP-like dynamics in the robot, the natural frequency of the SLIP model and the stride frequency should be matched. Equation (3) reveals that the former frequency is determined by the mass and the leg stiffness. Thus, while the robot mass is usually predetermined, the robot leg compliance is one of the key parameters to be tuned. This topic will be described separately in Sec. 4. In addition, it is desirable to have the robot stand without requiring motor power, which suggests a nonbackdrivable transmission system. As a result, a worm and worm gear pair is installed in the transmission system as well.

Turning the robot requires a separate mechanism because the designed transmission system has 1DOF and only allows the robot to move forward and backward. Thus, the robot is equipped with a carlike steering mechanism to control the direction of the forelegs as shown in Fig. 2. With these two DOFs, the robot is capable of walking, running, and turnings, just like ordinary wheeled vehicles moving on flat ground.

Figure 2 depicts a sketch of the final robot design and component arrangement. Motor power is transmitted to a long shaft installed in the fore-aft direction through a pair of spur gears. This shaft is mounted with three worms. Through the matched worm gears, the motor power is transmitted to the front, middle, and hind shafts mounted in the lateral direction. These shafts then connect to noncircular gears and then to the leg shafts, to create the desired speed variation of the legs as well as generate the phase difference between the two tripods. Note that the current design uses six pairs of noncircular gears, since they are mounted at the very end of the transmission system. Ideally, each tripod needs only one pair of noncircular gears if the gears are mounted at the beginning of the transmission system, before the motion splits to three legs of the tripod. In this morphology, most of the shafts move in the same pattern as the legs, which means extra power is required to accelerate/decelerate the shafts. In the design shown in Fig. 2, most of the shafts move at the same speed as the motor. This arrangement not only saves energy and reduces vibration but also uses the shafts as flywheels to stabilize the leg motion. In addition, this morphology preserves the possibility of using different leg rotation profiles on the legs of the same tripod.

The operator can remotely control the robot through a commercial radio-control (RC) transmitter–receiver pair designed for RC toys. The speed of the DC motor for robot driving can be varied by supplying different averaged voltage to the motor (pulse width modulation method), which is directly determined by the control bar on the transmitter. The motor speed is not feedback-controlled, so when the control bar is set at the same position, the motor speed may vary depending on the required torque and battery voltage.

Although the leg morphology and motion of the robot seem similar to that of RHex [9], there exists an important and fundamental difference. RHex is a typical example of a "mechanism less" system, whose legs are directly connected to the motor shafts. It is also the simplest form of hexapod in that category—containing only six active DOFs. Though the DOF of RHex is low compared to other legged robots, it can generate various behaviors such as stable walking [11], jogging [12], stair ascent/descent [40,41], pronking [42], bounding, bipedal running [43], self-righting [10], high-step climbing [13], and leaping [44,45]. Here, although the robot can only perform alternating tripod gaits owing to the trade-off of using a simple single-motor driving system, it has sufficient maneuverability and is good enough to negotiate various kinds of rough terrain. Its DOFs are reduced to a level comparable to general wheeled or tracked systems on the ground, yet with additional rough terrain negotiability. The motion constraint generated by the reduced DOF sometimes helps to support the force required for dynamic locomotion (e.g., centrifugal when the vehicle turns). Here, the 2DOF legged robot has a similar DOF arrangement as the 2DOF wheeled vehicle, so its control strategy is as simple as that of a wheeled one. This also implies that the actuation strategy of the legged robot in this morphology is "mechanical-based," unlike the "control-based" RHex. In short, the novelty and uniqueness of the designed robot lie in its simplicity of two active DOFs with a noncontrolled motor driving system, yet with the capability of dynamic ground locomotion and rough terrain negotiation.

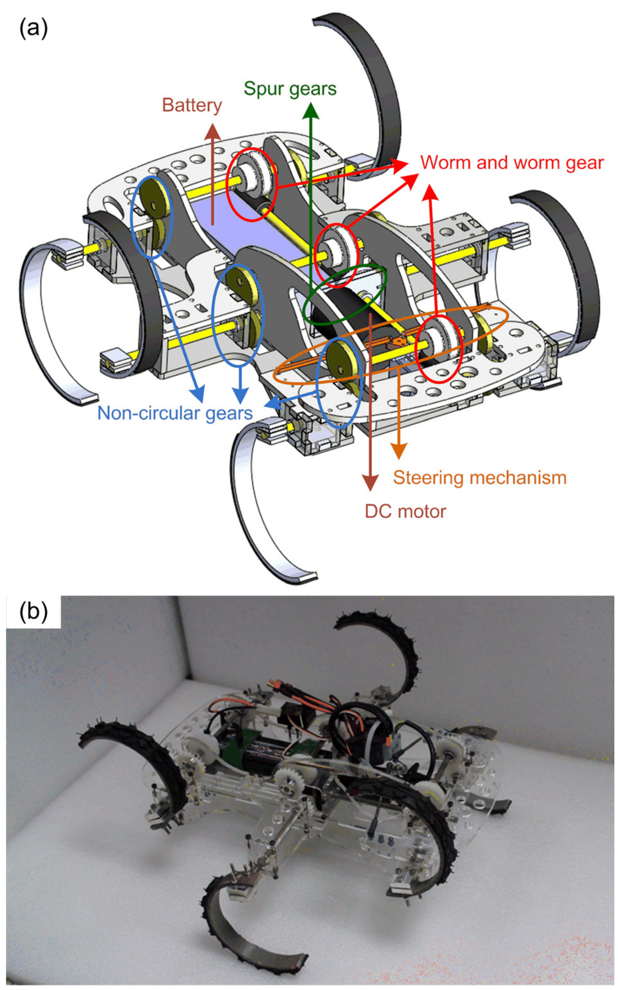

Fig. 2 The hexapod robot: (*a*) three-dimensional (3D) model which shows key components and (*b*) photo of the robot

3 Design of the Noncircular Gears

The transmission system described in Sec. 2 can be regarded as the main mechanism to create an alternating tripod gait, which requires two conditions. First, the legs' rotational speed should be varied so at least one tripod is usually configured in its stance posture, and the flight phase of the robot happens in between the stance postures of the two tripods. Second, two tripods need to have phase shift so they will contact the ground alternately. The latter condition can be easily achieved by configuring the transmission so that the tripods have a phase shift. To satisfy the first condition, a noncircular gear pair is adopted.

A gear is a type of transmission system which can continuously transmit rotational kinetic energy from one shaft to another. The kinematic motion of the gear pair is determined by the "imaginary" rolling circles, named pitch circles. Two pitch circles contact and roll with each other continuously. The rolling condition yields the same instant velocity, v, at interface, which can also be computed from both gears.

$$v = \omega_{\rm in} r_{\rm in} = \omega_{\rm out} r_{\rm out} \tag{5}$$

where $\omega_{\rm in}$ and $\omega_{\rm out}$ and $r_{\rm in}$ and $r_{\rm out}$ are the angular speeds and radii of the input and output gears, respectively. For an ordinary circular gear pair, the above four parameters are fixed. In contrast, for the noncircular gear pair, these four parameters are varied. Though the radii of two gears vary, the center distance of this gear pair, s, should be fixed

$$r_{\rm in} + r_{\rm out} = s \tag{6}$$

By combining Eqs. (5) and (6), the radius of the output gear can be parameterized as

$$r_{\rm out} = s/(1 + \omega_{\rm out}/\omega_{\rm in}) \tag{7}$$

which can be passively determined by the given center distance and speed ratio $\hat{\omega} = \omega_{\rm out}/\omega_{\rm in}$. In addition to the constraint defined in Eq. (7), the rotational speed of the gears should be matched as well, so the gear pair can rotate continuously. For simplicity, the rotational periods of both gears are set to be equal, so when the input gear rotates one turn, the output gear rotates one turn as well.

$$\int_0^p \omega_{\rm in} dt = \int_0^p \omega_{\rm out} dt = 2\pi \tag{8}$$

where p is the period of the gear. Note that the period of the gear can also be designed to be the integer multiple of the other one. (For example, one turn of the input gear yields a half turns or two turns of the output gear.) Setting one-turn-to-one-turn mapping is for simplicity. In addition, one turn of the output gear is also set to map one turn of the leg, so the gear profile is a geometrical representation of the leg motion.

The speed profile of the gears which satisfies the constraints described above can be computed by using the normalized plot shown in Fig. 3(*a*), which uses speed ratio, $\hat{\omega}$, as the vertical axis and normalized time, $\hat{t} = t/p$, ranging from 0 to 1 as the horizontal axis. In this case, the input gear can be regarded as having unit speed, as the red solid line shown in the plot. Because both axes are normalized, the integration of the speed ratio with respect to the normalized period should be set to 1, which automatically satisfies the requirement of Eq. (8)

$$\int_0^1 \hat{\omega} d\hat{t} = 1 \tag{9}$$

In other words, if the output gear moves according to the red solid line shown in Fig. 3(*a*), it moves with the same rotation angle (and speed) as the input gear. When the input gear makes one turn, the output gear also makes one turn, and the integrated area under the red line is equal to 1. Equivalently, if the output gear moves according to the green dashed-dotted curve which has speed variation, then as long as the integrated area underneath is equal to 1, whenever the input gear makes one turn, the output gear makes one turn as well. In addition, the speed profile should be designed to create the tripod gait as described in Sec. 2: The leg in stance phase (i.e., θ_s) should move slowly and take no more than half of one period, and the leg in flight has to move fast, preparing for the next stance phase. The green dashed-dotted line segments shown in Fig. 3(*a*) depict the base speed profile of the output gear, $\hat{\omega}_g$, which includes four segments: low velocity region, acceleration region, high velocity region, and deceleration region. The integrated area at the first half of the period is roughly equal to θ_s shown in Fig. 1(*c*). The speed profile of the output gear, $\hat{\omega}$, is further smoothed using a Fourier series with three terms to reduce the dramatic acceleration and deceleration in transmission.

$$\begin{aligned} \omega_{\text{out}}(\hat{t}) &= \frac{1}{2}a_0 + \sum_{n=1}^{2} a_n \cos(2\pi n\hat{t}) + b_n \sin(2\pi n\hat{t}) \\ a_n &= 2\int_0^1 \hat{\omega}_g \omega_{\text{in}} \cos(2\pi \hat{t}) d\hat{t} \\ b_n &= 2\int_0^1 \hat{\omega}_g \omega_{\text{in}} \sin(2\pi \hat{t}) d\hat{t} \end{aligned} \tag{10}$$

and is shown in the blue dashed curve in Fig. 3(*a*). Because the Fourier series will not change the integral in one period, the area below the blue dashed curve is the same as that below the green line segments. Thus, as long as the base speed profile satisfies the constraint shown in Eq. (9), the gears will function as desired.

The detailed gear profile can then be generated based on the defined profile of the speed ratio shown in Fig. 3(*a*). First, pitch circles of the noncircular gear pair are generated. Unlike a pitch circle of the ordinary gear which has constant radius, the pitch radius of the noncircular gear varies. In order to generate the pitch circles of the gear pair numerically, an angle which parametrizes orientation of the input gear is defined (i.e., ranging from 0 to 2π). By using Eqs. (6), (7), and gear speed ratio shown in Fig. 3(*a*), the pitch radii of the input gear and output gear at each gear orientation can be computed. Thus, the complete pitch circles can be generated after this parameter sweeps its full range. Following that, the final teeth profiles based on the involute geometry can be generated [46]. The pitch circles and tooth profiles of the noncircular gear pair are plotted in Fig. 3(*b*).

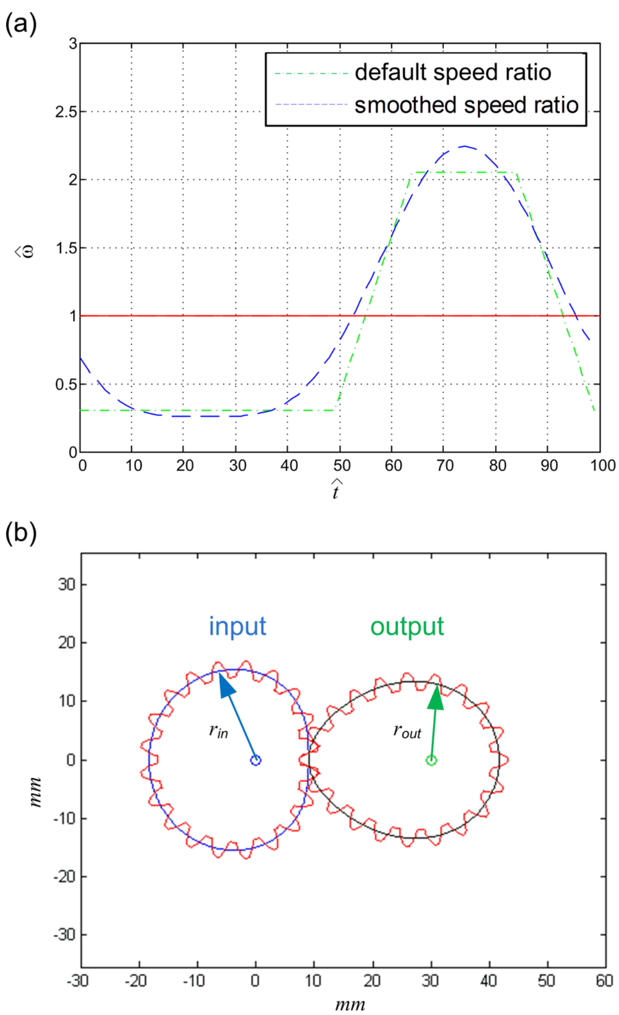

Fig. 3 Design of the noncircular gear pair. (*a*) The normalized angular speed profiles of the input gear (red solid line) and the output gear (base design: green dashed-dotted line segments; after smoothing: blue dashed curve). (*b*) The designed pitch circles and the final appearance of gear.

4 The Design of the Legs

The model-based design described in Sec. 2 suggests that the robot leg should act like a massless linear spring. The desired leg stiffness can be roughly estimated by the locomotion characteristics of animals with similar size and weight. According to Ref. [39], an animal weighing around 3 kg should have a body stride frequency f_s within a range of 3–4 Hz. Because the robot utilizes an alternating tripod gait, the leg stride frequency f_l should be half of the body stride frequency, about 1.5–2 Hz. Following this, the leg stiffness can be roughly estimated by using a 1DOF spring-mass model:

$$f_s = 2f_l = \frac{1}{2\pi}\sqrt{\frac{k}{m'}} \tag{11}$$

This is the same strategy adopted by biological research [19,20]. In addition, because tripod locomotion has three legs contacting the ground simultaneously, the stiffness of each leg should be one-third of the virtual leg stiffness, around 0.75 kN/m.

A commercial shock absorber for remote control cars (Fig. 4(*a*)) was employed in the first iteration of the robot leg. Though, in general, it has both spring and damper effects, by removing the oil inside the absorber piston it can perform like an idealized Hooke's law spring. Empirical evaluation confirms this behavior if the external forces acting on the absorber are close to the spring direction. However, the shock absorber does not work well when large lateral forces are involved. As a result, the compliant circular leg shown in Fig. 4(*b*) is adopted, the same morphology as the legs on RHex. As a side note, the same circular leg is also used on the leg-wheel transformable robot [47].

The compliant circular leg is a complex high-order system and its stiffness relative to the 1D virtual linear spring should be addressed. Owing to its rolling contact, the equivalent linear stiffness changes as the contact point changes. The force-deformation relation of the circular leg with different ground contact points spanning about 70 degrees were empirically measured, and the results are plotted in Fig. 4(*d*) with the angle definition shown in Fig. 4(*c*). This figure reveals that for each contact point, the stiffness is quite consistent, and this stiffness can be found by the linear regression method. However, the figure also shows that the 1D stiffness, k_{1D}, increases when the contact point moves close to the hip joint, varying from $0.7\,\mathrm{kN/m}$to $0.3\,\mathrm{kN/m}$ as shown in Fig. 4(*e*). Finally, based on this data, the stiffness of the effective virtual linear spring is chosen $1.1\,\mathrm{kN/m}$ to cover the stiffness values while the leg contacts the ground at a normal range (i.e., $\psi = -30$ deg to 10 deg). Note that the overall stiffness of the circular leg can be tuned to the range around $0.75\,\mathrm{kN/m}$ by reducing the width of the leg. However, we found that the empirical leg with this stiffness is very fragile and cannot survive in extensive experimental runs. Because the leg stride frequency can be operated at a higher value by increasing motor speed, the circular leg with equivalent linear spring of $1.1\,\mathrm{kN/m}$is adopted for our experimental work. According to Eq. (11), the new desired stride frequency is increased to 5 Hz, to keep the robot's motion close to its natural rhythm.

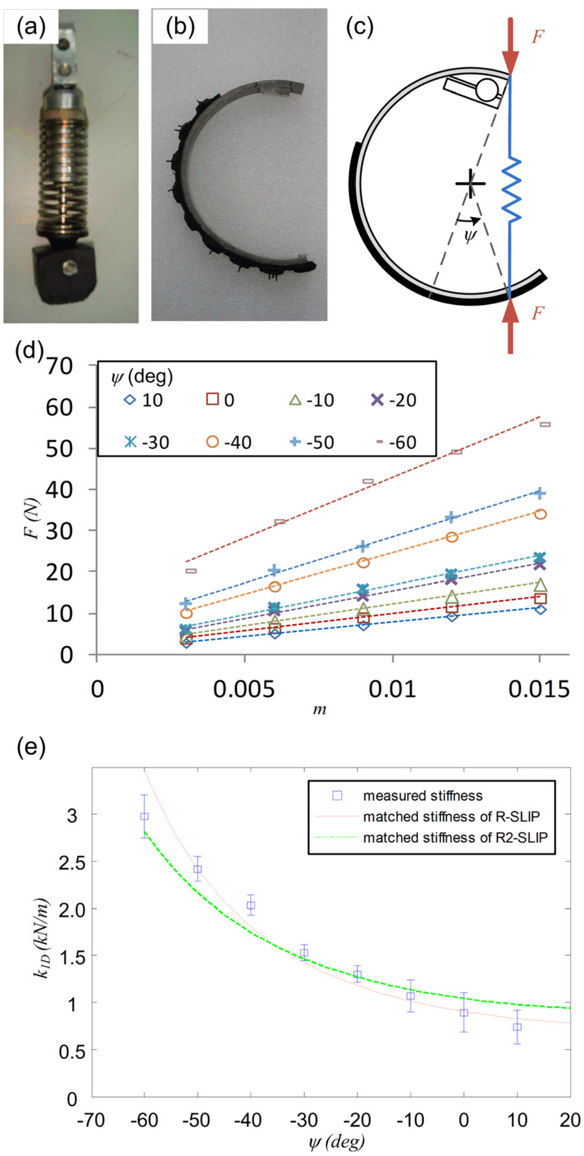

Fig. 4 Two types of legs used on the robot. (*a*) Linear spring leg and (*b*) compliant circular leg. (*c*) Method and notation of deriving equivalent linear spring stiffness of the compliant circular leg. (*d*) Plot of force versus deformation of the compliant circular leg with different contact points. (*e*) Plot of stiffness of the compliant circular leg versus different contact points. The matched torsion spring stiffness of the R-SLIP model and R2-SLIP is plotted in solid red curve and dashed green curve, respectively.

5 The Modified SLIP Models

The robot's locomotion is abstractly designed based on the dynamic motion of the SLIP model as described in Secs. 2–4. However, the adoption of the circular leg may result in different distal motion behavior in comparison to that of the SLIP model in the following aspects: First, the leg has rolling contact; and second, the equivalent linear stiffness changes as the contact point moves. Thus, the leg model needs to be revised to remedy this discrepancy generated by the use of a circular leg. Previously, we developed a SLIP model with rolling contact named R-SLIP as shown in Fig. 5(*a*) [33]. The R-SLIP model has four intrinsic parameters as listed in Table 1. By giving the same three ICs (α, β, v_{amp}) as those of the SLIP model, the dynamic locomotion of the R-SLIP model can be numerically simulated. The details are described in Ref. [33]. This configuration of the leg can incorporate the two characteristics of the circular leg described above which the SLIP model cannot provide. Thus, in the experimental evaluation of the robot, the R-SLIP model will be used as one of the dynamic models for performance comparison.

The revised version of R-SLIP, named R2-SLIP in Fig. 5(*b*), is also utilized as a model for performance comparison. R2-SLIP has a similar configuration to R-SLIP, except for the additional linear spring connecting the torsion spring and the circular rim. The idea behind the R2-SLIP model comes from making it capable of having 2D deformation as the circular leg does. The R-SLIP leg is a 1D reduced-order model whose deformation can only follow a specific pattern. In contrast, with the added linear spring whose motion is orthogonal to the torsional spring, the R2-SLIP leg can exhibit a 2D force-deflection pattern, and the deformation is decomposed into two springs in polar coordinates. Though the empirical force-deformation pattern of the circular leg may be considerably more complex than the model owing to its continuous deformable characteristic, R2-SLIP can provide the motion approximation without loss of mapping rank. The R2-SLIP model has five intrinsic parameters as shown in Table 1. By giving the same three ICs (α, β, v_{amp}) as those for the R-SLIP model, the dynamic locomotion of the R2-SLIP model can also be numerically simulated. The process of quantitative derivation of the R2-SLIP model is similar to that of the R-SLIP model reported in Ref. [33], and the details are described in the Appendix of this paper.

The dynamic performance of the physical robot will be compared to that of the SLIP, R-SLIP, and R2-SLIP models, so the parameters of these models should be correctly mapped to the robot specifications beforehand. The mapping of the mass (m) and the leg's geometrical characteristics (l of SLIP; l and r of R-SLIP; l_1 and r of R2-SLIP) are straightforward, and only the mapping of the stiffness needs to be developed. The mapping of the linear spring stiffness of SLIP is described in Sec. 4, which also served as a guideline for developing the leg stiffness of the robot. Thus,

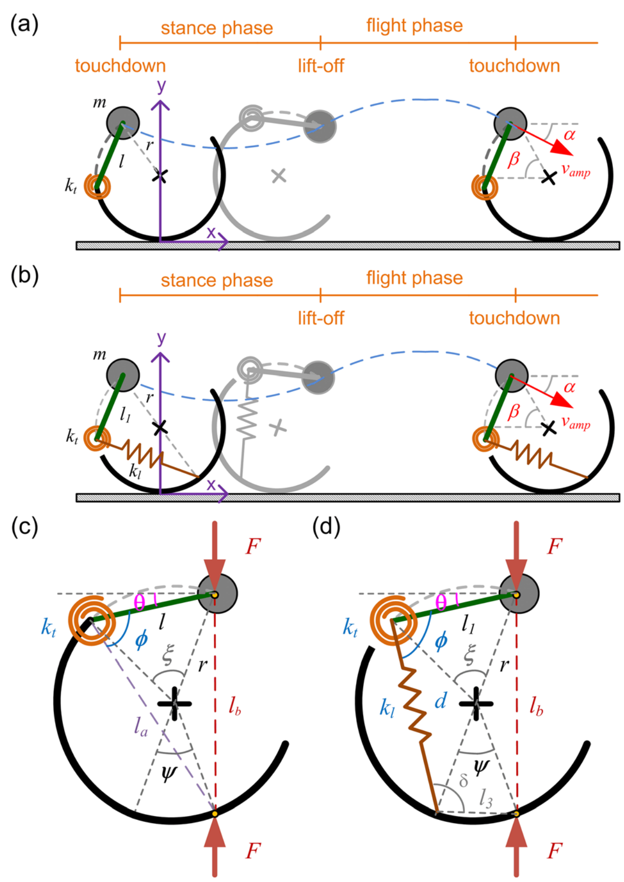

Fig. 5 (*a*) The R-SLIP and (*b*) R2-SLIP models with their intrinsic parameters, ICs, and motion profiles, respectively. The notations of the R-SLIP model (*c*) and the R2-SLIP model (*d*), which are used to determine the parameters of the models with best fit to the characteristics of the circular legs.

here the mapping of the stiffness of the R-SLIP and R2-SLIP models to the circular leg are addressed. The same force-deformation data of the circular leg shown in Fig. 4(*e*) are used, and the contact point is also parameterized by the symbol ψ.

Figure 5(*c*) depicts the notations for stiffness mapping between the R-SLIP model and the circular leg. The state of the torsional spring is parameterized by the symbol ϕ. The following equations can be defined based on geometrical relations:

$$
\begin{aligned}
l &= 2r\sin\left(\frac{\xi}{2}\right)\\
l_a &= 2r\sin\left(\frac{\pi-\xi+\psi}{2}\right)\\
\phi_0 &= \frac{\pi-\psi}{2}
\end{aligned}
\tag{12}
$$

Table 1 The model parameters and ICs

R-SLIP model parameters	R2-SLIP model parameters
Circular rim (r)	Circular rim (r)
Torsional spring stiffness (k_t)	Torsional spring stiffness (k_t)
	Linear spring stiffness (k_l)
Mass (m)	Mass (m)
Bar length (l)	Bar length (l_1)
Model ICs	
Landing angle (β)	
Touchdown speed (v_{amp})	
Touchdown angle (α)	

where the subscript 0 denotes the initial and undeformed condition. Because the leg is massless, the torque generated by the deformed torsional spring and the external forces are balanced in the static equilibrium

$$
Fl\cos(\theta) = (\phi_0-\phi)k_t \tag{13}
$$

with

$$
\begin{aligned}
\theta &= \cos^{-1}\left(\frac{l_a}{l_b}\sin(\phi)\right)\\
l_b &= \sqrt{l^2+l_a^2-2ll_a\cos(\phi)}
\end{aligned}
$$

The above equations allow us to numerically find unknowns θ and ϕ when the model is applied with a load F and given k_t and l (or ξ). Then, by letting k_t and l be free variables to be tuned, the best choices of k_t and l can be found by using the eight data sets shown in Fig. 4(*e*) and least squared error criteria. The figure also plots the stiffness (K_{ID}) versus ψ of the model with best parameters $k_t = 3.6$ (N m/rad) and $\xi = 71$ deg (red solid line). Except when $\psi = -60$ deg, the error at other ψs is generally less than 10%, especially at the commonly used region $\psi = -30$ deg to 10 deg.

Figure 5(*d*) depicts the notations for stiffness mapping between the R2-SLIP model and the circular leg. The states of the torsional spring and the linear spring are parameterized by the symbols ϕ and d, respectively. The following equations can be defined based on geometrical relations:

$$
\begin{aligned}
l_1 &= 2r\sin\left(\frac{\xi}{2}\right)\\
d_0 &= \sqrt{(2r)^2-l_1^2}\\
l_3 &= 2r\sin\left(\frac{\psi}{2}\right)\\
\phi_0 &= \frac{\pi}{2}
\end{aligned}
\tag{14}
$$

When the external forces F are applied, both springs are deformed in static equilibrium

$$
\begin{aligned}
Fl_1\cos(\theta) &= (\phi_0-\phi)k_t\\
F\sin(\phi-\theta) &= (d_0-d)k_l
\end{aligned}
\tag{15}
$$

To keep the forces acting along the same line, the following relationship should be held:

$$
\begin{aligned}
&-l_1\cos\theta + d\cos(\phi-\theta) + l_3\cos(\delta-\pi+\phi-\theta) = 0\\
&\text{with } \delta = \tan^{-1}\left(\frac{l_1}{d}\right) + \frac{\pi-\psi}{2}
\end{aligned}
\tag{16}
$$

Similar to the process described in the last paragraph, the unknowns θ, ϕ, and d can be derived when the model is applied with a load F and given k_t and l_1 (or ξ), and the deformed length l_b can then be found by the following equation:

$$
l_b = \sqrt{(l_x+l_1)^2+(l_y+l_3)^2-2(l_x+l_1)(l_y+l_3)\cos(-\pi+\phi+\delta)}
$$

with

$$
\begin{aligned}
l_x &= \frac{d\sin\delta}{-\sin(\phi+\delta)}\\
l_y &= \frac{d\sin\phi}{-\sin(\phi+\delta)}
\end{aligned}
\tag{17}
$$

Then, the best parameters k_t, k_1, and l_1 are found based on the criteria that the model with this specific set of parameters has the minimum summed percentage errors to the eight experimentally measured 1D stiffness (K_{ID}) of the circular leg as shown in Fig. 4(*e*). The best parameters are $k_t = 3.5(\mathrm{Nm/rad})$, $k_t = 4.5(\mathrm{kN/m})$, and $\xi = 55\,\mathrm{deg}$. The figure also plots the stiffness (K_{ID}) versus ψ of this model.

In comparison to the SLIP model, the R-SLIP and R2-SLIP models exhibit characteristics closer to the empirical circular leg such as rolling and variable linear stiffness. The dynamic motion of all three models will be compared to the robot. However, there still exists another major difference between the robot and the models: the energy characteristics. The models are energy conservative, so their locomotion is basically determined by the exchange of kinetic and potential energy. In contrast, the robot inputs power via a motor to overcome frictional losses. Thus, models with input torque and damping have been developed to address this issue [34,38,48]. This approach addresses the energy issue but also creates new challenges such as modeling the empirical torque control and placement of damping components which capture overall damping of the robot. These new issues are complex, particularly for this new and more sophisticated leg. Thus, instead of using torque and damping, the models are imposed with leg motion constraints as the solution to this energy issue. Since the robot has fixed motor characteristics and gear transmission systems, the motor speed can be fixed, yielding a specific leg rotational motion profile (i.e., $\theta(t), \dot{\theta}(t), \ddot{\theta}(t)$) with respect to the body frame. When the robot moves stably where its pitch variation is limited as shown in Fig. 1(*b*), the described leg profiles are equal to the leg profile with respect to the world frame as shown in Fig. 1(*c*). Therefore, when the robot's leg motion is mapped to the model's leg motion, one of the model leg's DOFs can be regarded as known (i.e., θ in all three models), and only the other state needs to be solved by the derived dynamic equations (i.e., l of the SLIP model, ϕ of the R-SLIP model, and ϕ and d of the R2-SLIP model). In summary, three models with this leg motion constraint will be used to evaluate their dynamic motion similarity to the empirical robot as well.

6 Robot Performance Evaluation

The robot shown in Fig. 2(*b*) was built for performance evaluation. It has a mass of 3.6 kg, and each leg (half-circular polyvinyl chloride and tire tread) has a mass of 0.035 kg. Figure 6(*a*) shows a snapshot of the robot negotiating an obstacle. A video is available as supplemental material. The legs correctly move according to the designed alternating tripod gait, so the robot can walk stably and smoothly. When the leg stride frequency increases, the robot's motion enters a dynamic region where it runs with alternating stance and flight phase as shown in Fig. 6(*b*). To quantitatively evaluate the dynamic behavior of the robot to the SLIP, R-SLIP, and R2-SLIP models, the robot was run at different stride frequencies under the ground truth measurement system as shown in Fig. 6(*c*). The system has two high-speed cameras (A504 k, Basler) installed on the top right and left sides of the experimental area to capture three LED markers mounted on top of the robot. The 3D positions of the markers can be reconstructed by two synchronized images captured by the cameras, running at 250 Hz. The robot's COM trajectories and body orientations versus time were recovered by the computed 3D coordinates of the three markers. A force plate (4060-07-1000, Bertec) was placed on the runway to record the force interaction between the robot and the ground.

Figure 7 plots the rotation speed of the designed profile (red with arrow) and empirical robot leg versus time while the robot is driven with different frequencies. The robot leg data are the derivation of the recorded data from an encoder installed on one of the legs. Because each subfigure contains data from several experimental runs, it is presented statistically with mean and standard deviation (vertical bars). The designed profile is computed from the transmission profile described in Sec. 3 with the assumption of

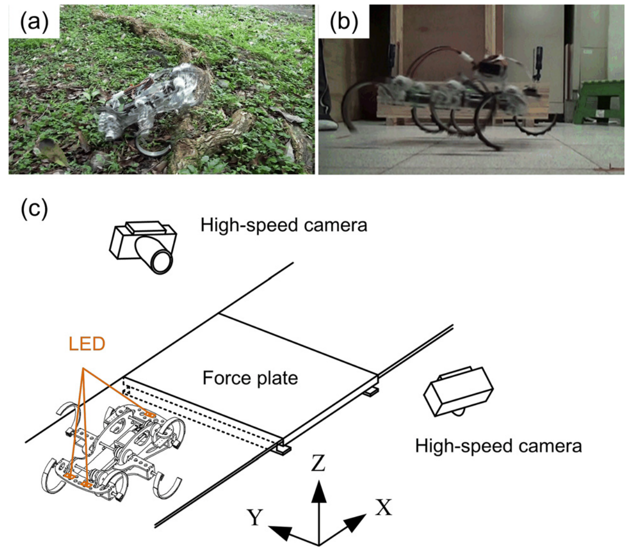

Fig. 6 Photos of the robot walking (*a*) and jogging (*b*). (*c*) Experimental setup for robot performance evaluation.

constant motor speed input. Because the empirical stride frequencies of the robot in each subfigure vary slightly, the desired leg speed also has variation, and the data are presented statistically with mean and standard deviation. The plotted range of the designed profile equals the range of the robot stance phase. This figure is the baseline comparison to evaluate whether or not the robot leg moves according to the designed profile. The figure reveals that in most cases the leg moves in the predicted manner. The largest error takes place when the leg touches the ground. At this moment, the torque required to keep the body moving forward increases suddenly. This phenomenon is clearly observed when the robot stride frequency is low, where the robot has less forward momentum. After the initial ground engagement, the leg can quickly recover to its designed rotational speed. This figure confirms that the driving motor is most likely powerful enough to sustain the required torque variation during locomotion, so the robot leg can indeed move according to the designed profile. This is important because the designed leg profile is used as the motion constraint criteria in the models with leg motion constraint (i.e., regulated model).

To systematically evaluate the behavior of the robot, the robot was run 32 times with various stride frequencies from 2.6 Hz to 9.2 Hz. The data of the robot were grouped into three frequency

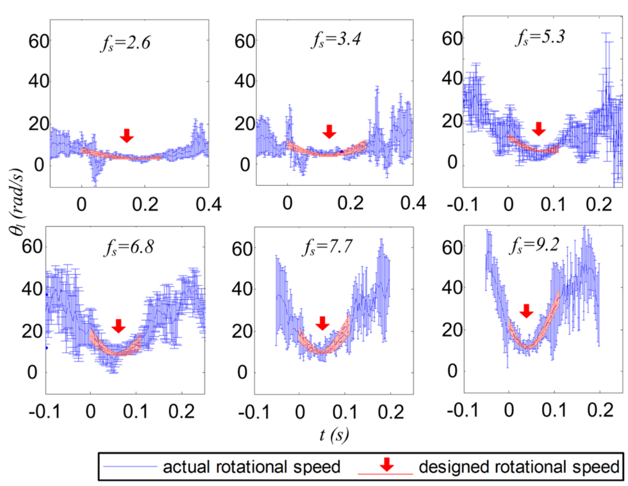

Fig. 7 Mean and standard deviations of the legs' actual (blue) and designed (red with arrow) rotational speeds

groups for performance analysis in a statistical manner, and the mean and standard deviations of the frequencies in the groups are 3.6(0.3) Hz, 5.2(0.4) Hz, and 9.1(0.4) Hz, respectively. The displacement data were measured by a camera system, and the velocity data derived from this data without any post processing (i.e., filter). The acceleration data are computed from the force data with division to mass.

Figure 8 plots the steady-state displacement, velocity and acceleration of the robot COM in the fore/aft (x) and vertical (z) directions versus time with the described frequency groups. The vertical reference is set on the ground, and the nominal height of the robot COM 0.099 m is plotted as the reference as well. The time duration covers one stride period. The robot data shown in blue are presented in a statistical manner with mean and standard deviation (vertical bars). In addition, Fig. 9 plots the robot COM trajectories (blue) in the sagittal plane. Several observations can be drawn based on these two figures: (i) The robot with low stride frequency 3.6(0.3) Hz shown in Fig. 8(*a*) exhibits behavior close to the slow tripod walking where the robot's COM in the vertical direction has an increase–decrease profile. (ii) In contrast, the

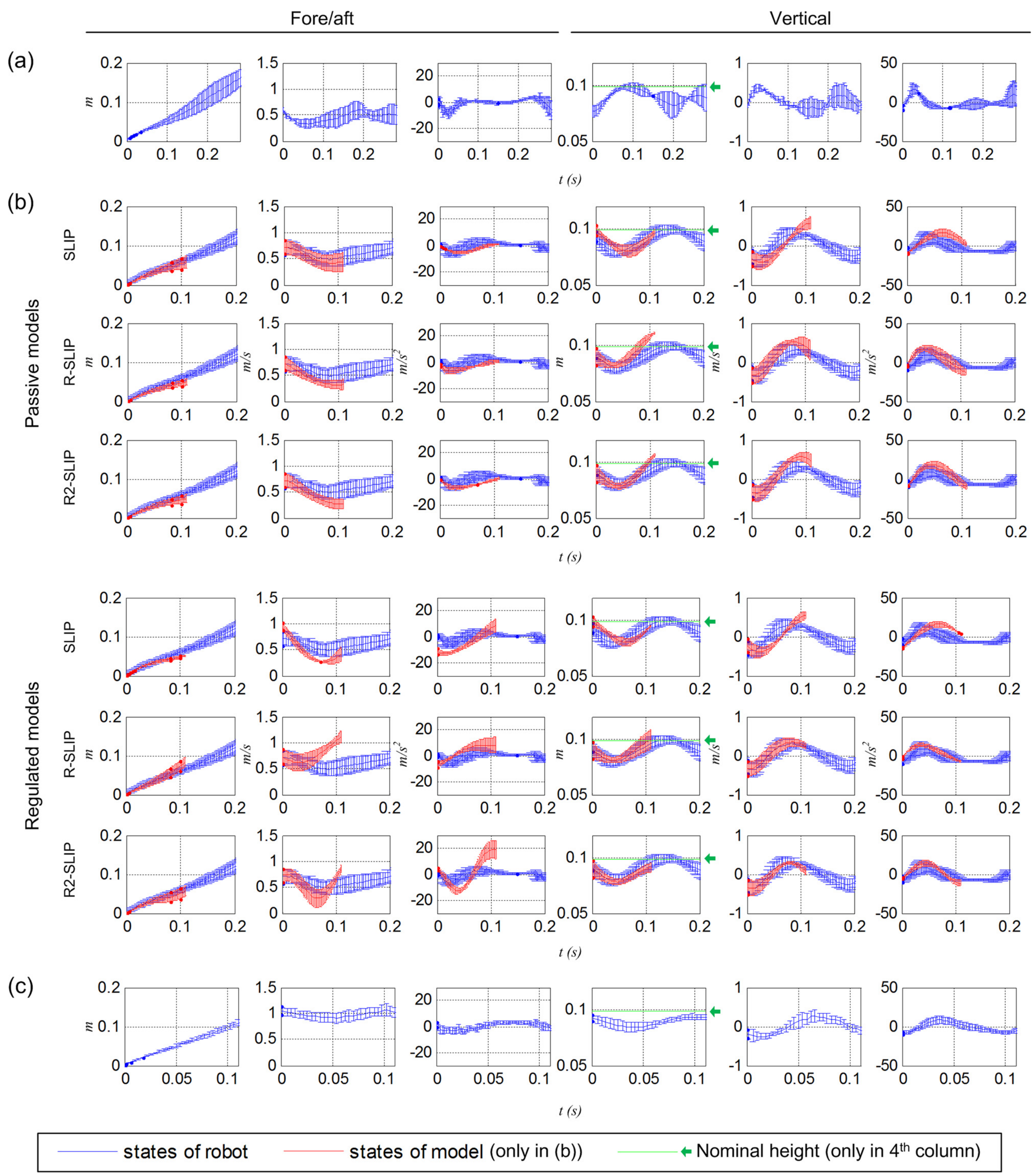

Fig. 8 The states of the robot (blue) and models (red). The robot is operated with different stride frequencies: 3.6(0.3) Hz in (*a*), 5.2(0.4) Hz in (*b*), and 9.1(0.4) Hz in (*c*).

robot with middle stride frequency 5.2(0.4) Hz shown in Fig. 8(*b*) (also the frequency designed for running described in Sec. 4) exhibits behavior close to dynamic running, where the robot's COM in the vertical direction has a decrease–increase profile, matching the leg spring's single compression-release pattern. In addition, the robot with this stride frequency has larger landing angle in comparison with the robot with low stride frequency shown in Fig. 8(*a*), so the initial COM heights in both cases are different. (iii) The robot with high stride frequency, 9.1(0.4) Hz, exhibits behavior similar to tripod walking. The tripod of the robot at this frequency has less effect on the overall robot motion, and on this occasion the robot's COM maintains a similar height during locomotion. (iv) The forward speed of the robot increases as the stride frequency increases. The mean (std) speed of the robot with three groups of frequencies are 0.49(0.06), 0.62(0.06), and 1.01(0.06) m/s, respectively. In short, a robot with the right frequency range can excite its dynamic behavior, and one in another frequency range can perform ordinary tripod walking. The walking and running behaviors can also be actively and easily initiated by changing the voltage supplied to the driving motor of the robot, where the higher voltage yields a higher stride frequency. In addition and higher forward speed change.

To further evaluate the dynamic behavior of the robot with a stride frequency of 5.2(0.4) Hz, the robot data were compared with the SLIP, R-SLIP, and R2-SLIP models' data, both without and with leg motion constraint (i.e., passive versus regulated model). The touch-down and lift-off moments of the robot are determined by the vertical ground reaction force data, and this information is used for synchronization with the model data. Because the touchdown conditions of the robot vary slightly for different strides and runs, the models are simulated according to the measured ICs. Thus, the model data have variations as well. Likewise, their mean and standard deviations are used for performance analysis. For comparison, Fig. 8(*b*) plots the displacement, velocity, and acceleration of the passive model and regulated model in fore/aft (x) and vertical (z) directions versus time, respectively. Likewise, Fig. 9(*b*) plots the mass trajectories of the models in the sagittal plane. The root mean squared (RMS) errors between the robot and the models in fore/aft vertical, and planar displacements and velocities are listed in Table 2. The former two errors can be regarded as the statistical results of the data shown in the first and fourth columns of Fig. 8(*b*).

First, we consider the dynamic states such as velocity and acceleration. Figure 8(*b*) reveals that the R-SLIP and R2-SLIP models are a better match to the robot than the SLIP model, where the latter has a larger variation in motion trend. Regarding the first two models, the figure also reveals that the data in the vertical direction have a better match, and that in the fore/aft direction there is some discrepancy. This can be explained by the ground slippage effect. The presented data in displacement, velocity, and acceleration are derivatively and integratively related, so velocity (the middle datum) is used for explanation. The forward velocities of the passive models are generally lower than that of the robot because the leg regulation powered by the motor is ignored. On the other hand, the forward velocities of the regulated models are generally faster than that of the robot, mainly because the empirical friction force is not sufficient to help the robot achieve the desired acceleration in the second half of the stride period. Thus, the empirical robot's forward velocity lies between the velocity of the passive model and the regulated model. In contrast, the motion in the vertical direction is less affected by friction, so the motion trends of the robot and models match reasonably well. The unmodeled friction effect makes the robot's forward speed slower than expected because the ground contact point does not move forward owing to slippage. This empirical fact favors the SLIP model because its ground contact point is supposedly fixed. As a result, though the SLIP model does not match the dynamic details as the other two models as shown in Fig. 8(*b*), the displacement state of the SLIP model appears to have a reasonable match as shown in Fig. 9(*b*). The planar RMS errors shown in Table 2 reveal that the error is smaller than that of the R-SLIP model and is comparable to that of the R2-SLIP model. Considering only the displacement state, Table 2 reveals that the R2-SLIP has the best match to the robot behavior on most occasions. In summary, if the modeling is acting at a very abstract level and the COM trajectory is the most important state to consider, then the SLIP model is usually sufficient to satisfy this requirement. On the other hand, if the modeling is taken to a deeper level where the detail dynamics are addressed, the R-SLIP and R2-SLIP models are better choices since they fundamentally catch the dynamic properties of the compliant leg better. Moreover, if both displacement and dynamics are considered, the R2-SLIP model is the most adequate choice. On the other hand, if the controller law is to be model-based, the R-SLIP model may be the better choice since it catches the dynamics with a model structure that is simpler than that of the R2-SLIP.

7 Conclusion

We report on the design and implementation of a bio-inspired hexapod robot, which merges the simple morphology of RHex with bio-inspired tripod gaits and circular legs as well as the single-motor transmission strategy of iSprawl. The uses of a noncircular gear pair and a worm and worm gear pair are confirmed to be effective in generating tripod locomotion and energy-efficient standing posture of the robot. The robot can be operated like an ordinary vehicle, yet it can negotiate obstacles because of large ground clearance created by the legs' aerial phase. In addition, by appropriately using the passive dynamic strategy where the mass, leg stiffness, and stride frequency of the robot are matched to a reduced-order dynamic model's natural rhythm, the robot can initiate running motion with a flight phase. The experimental evaluation of the robot also reveals that its motion changes from slow walking, to running, and then to fast walking when the stride frequency increases, and the robot's forward speed increases accordingly.

The success of this minimally actuated legged platform underscores the importance of the passive dynamics created by the interplay between the rhythmic actuation, compliant legs, and contact with the ground. Since the shape of the legs dictates the system's behavior, an accurate, yet simple, dynamic model which

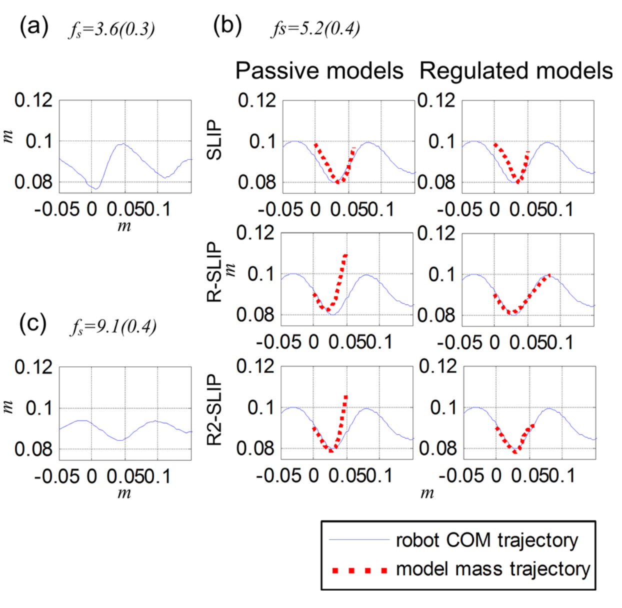

Fig. 9 The robot COM trajectories (blue solid) and model mass trajectories (red dashed). The robot is operated with different stride frequencies: 3.6(0.3) Hz in (*a*), 5.2(0.3) Hz in (*b*), and 9.1(0.4) Hz in (*c*).

Table 2 The RMS errors between the robot and the models

	SLIP	R-SLIP	R2-SLIP
Displacement in fore/aft direction (mm)			
Passive	4.21 (2.87)	5.27 (2.06)	4.69 (2.71)
Regulated	4.93 (1.73)	5.91 (4.53)	4.87 (3.80)
Displacement in vertical direction (mm)			
Passive	5.05 (1.57)	7.76 (2.01)	4.08 (2.43)
Regulated	5.37 (2.66)	4.28 (2.67)	4.61 (1.35)
Planar displacement (mm)			
Passive	6.60 (2.22)	9.54 (2.08)	6.66 (2.39)
Regulated	8.00 (0.84)	7.92 (3.89)	7.32 (2.20)
Velocity in fore/aft direction (m/s)			
Passive	0.151 (0.0539)	0.166 (0.0639)	0.165 (0.0940)
Regulated	0.395 (0.124)	0.235 (0.128)	0.192 (0.0895)
Velocity in vertical direction (m/s)			
Passive	0.176 (0.0561)	0.209 (0.0796)	0.172 (0.0656)
Regulated	0.185 (0.0783)	0.142 (0.0763)	0.117 (0.0479)
Planar velocity (m/s)			
Passive	0.233(0.767)	0.276 (0.0648)	0.247 (0.0856)
Regulated	0.445 (0.105)	0.286 (0.118)	0.233 (0.0725)

accounts for the leg geometry is desired. To evaluate the fidelity of reduced-order models in capturing these locomotive dynamics, the running performance of the robot is compared to three reduced-order models. The robot's COM trajectory in the sagittal plane has the highest similarity to the SLIP model, but the R-SLIP and R2-SLIP models catch the dynamic details of the locomotion better. Considering all states, the new R2-SLIP model may be the best tool to evaluate and inform future leg design efforts, which will, in turn, enable more capable and agile running robots—whether they have many or few actuated DOFs in their legs.

Acknowledgment

The authors would like to thank undergraduate students Meng-Ching Tsai, Fang-Yu Liang, Ya-Hsun Hsueh, and Yi-Chung Lan for helping to build the prototype of the robot. The original work was part of a start-up effort by the authors. This work was supported by the National Science Council (NSC), Taiwan, under Contract Nos. 99-2815-C-002-004-E and 100-2628-E-002-021-MY3, and the Ministry of Science and Technology (MoST), Taiwan, under Contract No. MOST 103-2221-E-002-091-MY3.

Appendix: Derivation of the R2-SLIP Model

Figure 5(*b*) depicts the configuration of the R2-SLIP model, and its motion includes stance and flight phases as the SLIP or R-SLIP models do. The process of deriving its dynamic model is similar to that of the SLIP or R-SLIP model, except for the over-constraint condition. To remedy this, a small mass is installed at the junction of the linear spring and the torsion spring, so the dynamics of the model become solvable. Note that the mass m of the R2-SLIP model or the R-SLIP model usually represents the robot body mass, and the small mass of the R2-SLIP model represents the leg mass. When the model is mapped to the robot with tripod locomotion, the stiffness and mass of the model leg should be triple of the individual robot leg.

The dynamic behavior of R2-SLIP model in stance phase can be derived by the Lagrangian method. The generalized coordinates include the length d and the two angles θ and ϕ as shown in Fig. 5(*d*). Assuming the leg rolls on the ground without sliding, the Cartesian coordinates of the body mass, (x_b, y_b), and leg mass, (x_l, y_l), can be represented as

$$\begin{aligned}
x_b &= r(\phi - \theta + \theta_0) + r\cos(\phi - \theta + \zeta) - d\cos(\phi - \theta) + l_1\cos\theta \\
y_b &= r - r\sin(\phi - \theta + \zeta) + d\sin(\phi - \theta) + l_1\sin\theta \\
x_l &= r(\phi - \theta - \phi_0 + \theta_0) + r\cos(\phi - \theta + \zeta) - d\cos(\phi - \theta) \\
y_l &= r - r\sin(\phi - \theta + \zeta) + d\sin(\phi - \theta)
\end{aligned} \tag{A1}$$

where the angle ζ is included by the linear spring and the line connecting the center of the circular rim and the position where the linear spring is attached to. The subscript 0 of θ and ϕ indicates the natural configuration of the model when the springs are not compressed. The kinetic energy T and potential energy V are

$$\begin{aligned}
T &= \frac{1}{2}m_b(\dot{x}_b^2 + \dot{y}_b^2) + \frac{1}{2}m_l(\dot{x}_l^2 + \dot{y}_l^2) \\
V &= m_b g(r - r\sin(\phi - \theta + \zeta) + d\sin(\phi - \theta) + l_1\sin\theta) \\
&\quad + m_l g(r - r\sin(\phi - \theta + \zeta) + d\sin(\phi - \theta)) \\
&\quad + \frac{1}{2}k_T(\phi_0 - \phi)^2 + \frac{1}{2}k_l(d_0 - d)^2
\end{aligned} \tag{A2}$$

Next, the equation of motions can be derived as

$$\begin{aligned}
\frac{d}{dt}\left(\frac{\partial}{\partial\dot{\theta}}\right) - \frac{\partial T}{\partial\theta} + \frac{\partial V}{\partial\theta} &= 0 \\
\frac{d}{dt}\left(\frac{\partial T}{\partial\dot{\phi}}\right) - \frac{\partial T}{\partial\phi} + \frac{\partial V}{\partial\phi} &= 0 \\
\frac{d}{dt}\left(\frac{\partial T}{\partial\dot{d}}\right) - \frac{\partial T}{\partial d} + \frac{\partial V}{\partial d} &= 0
\end{aligned} \tag{A3}$$

With the given ICs, the dynamic motion of the R2-SLIP model in its stance phase can be computed numerically. The motion of the model in its flight phase is ballistic. Similarly, in the regulated case where the leg orientation is regarded as known, only the states ϕ and d need to be computed.

References

[1] Raibert, M., 2000, *Legged Robots That Balance*, MIT, Cambridge, MA.
[2] Poulakakis, I., Smith, J. A., and Buehler, M., 2005, "Modeling and Experiments of Untethered Quadrupedal Running With a Bounding Gait: The Scout II Robot," Int. J. Rob. Res., **24**(4), pp. 239–256.
[3] Buehler, M., Battaglia, R., Cocosco, A., Hawker, G., Sarkis, J., and Yamazaki, K., 1998, "SCOUT: A Simple Quadruped That Walks, Climbs, and Runs," IEEE International Conference on Robotics and Automation (ICRA), Leuven, Belgium, May 16–20, pp. 1707–1712.
[4] Kimura, H., Fukuoka, Y., and Cohen, A. H., 2007, "Adaptive Dynamic Walking of a Quadruped Robot on Natural Ground Based on Biological Concepts," Int. J. Rob. Res., **26**(5), pp. 475–490.
[5] Fukuoka, Y., Kimura, H., and Cohen, A. H., 2003, "Adaptive Dynamic Walking of a Quadruped Robot on Irregular Terrain Based on Biological Concepts," Int. J. Rob. Res., **22**(3–4), pp. 187–202.
[6] Cham, J. G., Karpick, J. K., and Cutkosky, M. R., 2004, "Stride Period Adaptation of a Biomimetic Running Hexapod," Int. J. Rob. Res., **23**(2), pp. 141–153.
[7] Kim, S., Clark, J. E., and Cutkosky, M. R., 2006, "iSprawl: Design and Tuning for High-Speed Autonomous Open-Loop Running," Int. J. Rob. Res., **25**(9), pp. 903–912.
[8] Cham, J. G., Bailey, S. A., Clark, J. E., Full, R. J., and Cutkosky, M. R., 2002, "Fast and Robust: Hexapedal Robots Via Shape Deposition Manufacturing," Int. J. Rob. Res., **21**(10–11), pp. 869–882.
[9] Saranli, U., Buehler, M., and Koditschek, D. E., 2001, "RHex: A Simple and Highly Mobile Hexapod Robot," Int. J. Rob. Res., **20**(7), pp. 616–631.
[10] Saranli, U., Rizzi, A. A., and Koditschek, D. E., 2004, "Model-Based Dynamic Self-Righting Maneuvers for a Hexapedal Robot," Int. J. Rob. Res., **23**(9), pp. 903–918.
[11] Lin, P. C., Komsuoglu, H., and Koditschek, D. E., 2005, "A Leg Configuration Measurement System for Full-Body Pose Estimates in a Hexapod Robot," IEEE Trans. Rob., **21**(3), pp. 411–422.
[12] Lin, P. C., Komsuoglu, H., and Koditschek, D. E., 2006, "Sensor Data Fusion for Body State Estimation in a Hexapod Robot With Dynamical Gaits," IEEE Trans. Rob., **22**(5), pp. 932–943.
[13] Chou, Y. C., Yu, W. S., Huang, K. J., and Lin, P. C., 2012, "Bio-Inspired Step-Climbing in a Hexapod Robot," Bioinspiration Biomimetics, **7**(3), p. 036008.
[14] Burden, S., Clark, J., Weingarten, J., Komsuoglu, H., and Koditschek, D. E., 2007, "Heterogeneous Leg Stiffness and Roll in Dynamic Running," IEEE

International Conference on Robotics and Automation (ICRA), Rome, Apr. 10–14, pp. 4645–4652.
[15] Galloway, K. C., Clark, J. E., Yim, M., and Koditschek, D. E., 2011, "Experimental Investigations Into the Role of Passive Variable Compliant Legs for Dynamic Robotic Locomotion," IEEE International Conference on Robotics and Automation (ICRA), Shanghai, May 9–13, pp. 1243–1249.
[16] Haldane, D. W., Peterson, K. C., Garcia Bermudez, F. L., and Fearing, R. S., 2013, "Animal-Inspired Design and Aerodynamic Stabilization of a Hexapedal Millirobot," IEEE International Conference on Robotics and Automation (ICRA), Karlsruhe, Germany, May 6–10, pp. 3279–3286.
[17] Alexander, R. M., 1988, *Elastic Mechanisms in Animal Movement*, Cambridge University Press, Cambridge, UK.
[18] McMahon, T. A., 1988, "Elastic Mechanisms in Animal Moment—Alexander, R. M.," Nature, **336**(6199), p. 530.
[19] Blickhan, R., 1989, "The Spring Mass Model for Running and Hopping," J. Biomech., **22**(11–12), pp. 1217–1227.
[20] Holmes, P., Full, R. J., Koditschek, D., and Guckenheimer, J., 2006, "The Dynamics of Legged Locomotion: Models, Analyses, and Challenges," SIAM Rev., **48**(2), pp. 207–304.
[21] Full, R. J., and Koditschek, D. E., 1999, "Templates and Anchors: Neuromechanical Hypotheses of Legged Locomotion on Land," J. Exp. Biol., **202**(23), pp. 3325–3332, available at: http://jeb.biologists.org/content/202/23/3325.full.pdf+html
[22] Altendorfer, R., Moore, N., Komsuolu, H., Buehler, M., Brown, H. B., McMordie, D., Saranli, U., Full, R., and Koditschek, D. E., 2001, "RHex: A Biologically Inspired Hexapod Runner," Auton. Rob., **11**(3), pp. 207–213.
[23] Huang, C. K., Huang, K. J., and Lin, P. C., 2013, "Rolling SLIP Model Based Running on a Hexapod Robot," IEEE/RSJ International Conference on Intelligent Robots and Systems (IROS), Tokyo, Nov. 3–7, pp. 5608–5614.
[24] Huang, K. J., Chen, S. C., Tsai, M. C., Liang, F. Y., Hsueh, Y. H., and Lin, P. C., 2012, "A Bio-Inspired Hexapod Robot With Noncircular Gear Transmission System," IEEE/ASME International Conference on Advanced Intelligent Mechatronics (AIM), Kachsiung, Taiwan, July 11–14, pp. 33–38.
[25] Abbas, J., and Full, R., 2000, "Neuromechanical Interaction in Cyclic Movements," *Biomechanics and Neural Control of Posture and Movement*, J. Winters and P. Crago, eds., Springer, New York, pp. 177–191.
[26] Full, R., Farley, C., and Winters, J., 2000, "Musculoskeletal Dynamics in Rhythmic Systems: A Comparative Approach to Legged Locomotion," *Biomechanics and Neural Control of Posture and Movement*, J. Winters, and P. Crago, eds., Springer, New York, pp. 192–205.
[27] Spenko, M. J., Haynes, G. C., Saunders, J. A., Cutkosky, M. R., Rizzi, A. A., Full, R. J., and Koditschek, D. E., 2008, "Biologically Inspired Climbing With a Hexapedal Robot," J. Field Rob., **25**(4–5), pp. 223–242.
[28] Poulakakis, I., and Grizzle, J. W., 2009, "The Spring Loaded Inverted Pendulum as the Hybrid Zero Dynamics of an Asymmetric Hopper," IEEE Trans. Autom. Control, **54**(8), pp. 1779–1793.
[29] Chen, X., Gao, F., Qi, C., Tian, X., and Zhang, J., 2014, "Spring Parameters Design for the New Hydraulic Actuated Quadruped Robot," ASME J. Mech. Rob., **6**(2), p. 021003.
[30] Galloway, K. C., Clark, J. E., and Koditschek, D. E., 2013, "Variable Stiffness Legs for Robust, Efficient, and Stable Dynamic Running," ASME J. Mech. Rob., **5**(1), p. 011009.
[31] Rummel, J., and Seyfarth, A., 2008, "Stable Running With Segmented Legs," Int. J. Rob. Res., **27**(8), pp. 919–934.
[32] Jae Yun, J., and Clark, J. E., 2009, "Dynamic Stability of Variable Stiffness Running," IEEE International Conference on Robotics and Automation (ICRA), Kobe, Japan, May 12–17, pp. 1756–1761.
[33] Huang, K. J., Huang, C. K., and Lin, P. C., 2014, "A Simple Running Model With Rolling Contact and Its Role as a Template for Dynamic Locomotion on a Hexapod Robot," Bioinspiration Biomimetics, **9**(4), p. 046004.
[34] Seipel, J. E., and Holmes, P., 2007, "A Simple Model for Clock-Actuated Legged Locomotion," Regular Chaotic Dyn., **12**(5), pp. 502–520.
[35] Jae Yun, J., and Clark, J. E., 2011, "Effect of Rolling on Running Performance," IEEE International Conference on Robotics and Automation (ICRA), Shanghai, May 9–13, pp. 2009–2014.
[36] Ankaralı, M. M., Saygıner, E., Yazıcıoğlu, Y., Saranli, A., and Saranli, U., 2012, "A Dynamic Model of Running With a Half-Circular Compliant Leg," 15th International Conference on Climbing and Walking Robots (CLAWAR), Baltimore, MD, July 23–26, pp. 425–432.
[37] Peuker, F., Seyfarth, A., and Grimmer, S., 2012, "Inheritance of SLIP Running Stability to a Single-Legged and Bipedal Model With Leg Mass and Damping," 4th IEEE RAS & EMBS International Conference on Biomedical Robotics and Biomechatronics (BioRob), Rome, June 24–27, pp. 395–400.
[38] Ankarali, M. M., and Saranli, U., 2011, "Control of Underactuated Planar Pronking Through an Embedded Spring-Mass Hopper Template," Auton. Rob., **30**(2), pp. 217–231.
[39] Heglund, N. C., Taylor, C. R., and McMahon, T. A., 1974, "Scaling Stride Frequency and Gait to Animal Size: Mice to Horses," Science, **186**(4169), pp. 1112–1113.
[40] Moore, E. Z., Campbell, D., Grimminger, F., and Buehler, M., 2002, "Reliable Stair Climbing in the Simple Hexapod RHex," Proceedings of the International Conference on Robotics and Automation, pp. 2222–2227.
[41] Campbell, D., and Buehler, M., 2003, "Stair Descent in the Simple Hexapod RHex," International Conference on Robotics and Automation (ICRA '03), Taipei, Taiwan, Sept. 14–19, pp. 1380–1385.
[42] McMordie, D., and Buehler, M., 2001, "Towards Pronking With a Hexapod Robot," 4th International Conference on Climbing and Walking Robots and the Support Technologies for Mobile Machines, Karlsruhe, Germany, Sept. 24–26, pp. 659–666.
[43] Neville, N., Buehler, M., and Sharf, I., 2006, "A Bipedal Running Robot With One Actuator Per Leg," IEEE International Conference on Robotics and Automation (ICRA 2006), Orlando, May 15–19, pp. 848–853.
[44] Johnson, A. M., and Koditschek, D. E., 2013, "Toward a Vocabulary of Legged Leaping," IEEE International Conference on Robotics and Automation (ICRA), Karlsruhe, Germany, May 6–10, pp. 2553–2560.
[45] Chou, Y. C., Huang, K. J., Yu, W. S., and Lin, P. C., 2015, "Model-Based Development of Leaping in a Hexapod Robot," IEEE Trans. Rob., **31**(1), pp. 40–54.
[46] Litvin, F. L., Fuentes-Aznar, A., Gonzalez-Perez, I., and Hayasaka, K., 2009, *Noncircular Gears: Design and Generation*, Cambridge University Press, New York.
[47] Chen, S. C., Huang, K. J., Chen, W. H., Shen, S. Y., Li, C. H., and Lin, P. C., 2014, "Quattroped: A Leg-Wheel Transformable Robot," IEEE/ASME Trans. Mechatronics, **19**(2), pp. 730–742.
[48] Jun, J. Y., and Clark, J. E., 2012, "A Reduced-Order Dynamical Model for Running With Curved Legs," IEEE International Conference on Robotics and Automation (ICRA), St. Paul, MN, May 14–18, pp. 2351–2357.